Aerosol Dynamics in the Near Field of the SCoPEx Stratospheric Balloon Experiment

C. M. Golja[1], L. W. Chew[2], J. A. Dykema[1], and D. W. Keith[1]

[1] Harvard John A. Paulson School of Engineering and Applied Sciences, Cambridge, MA, USA.
[2] Massachusetts Institute of Technology, Department of Mechanical Engineering, Cambridge, MA, USA.

Corresponding author: Colleen Golja (cgolja@g.harvard.edu)

Key Points:

- Improved models of stratospheric solar geoengineering require accurate predictions of aerosol formation in aircraft wakes.
- A new 3D aerosol microphysics model predicts distribution and optical density of sulfate and calcite aerosols in the SCoPEx propeller wake.
- This model is a step towards quantitative comparison between models and measurements of aerosol formation in stratospheric wakes.

This article has been accepted for publication and undergone full peer review but has not been through the copyediting, typesetting, pagination and proofreading process, which may lead to differences between this version and the Version of Record. Please cite this article as doi: 10.1029/2020JD033438.

Abstract

Stratospheric aerosol injection (SAI) might alleviate some climate risks associated with accumulating greenhouse gases. Reduction of specific process uncertainties relevant to the distribution of aerosol in a turbulent stratospheric wake is necessary to support informed decisions about aircraft deployment of this technology. To predict aerosol size distributions we apply microphysical parameterizations of nucleation, condensation and coagulation to simulate an aerosol plume generated via injection of calcite powder or sulphate into a stratospheric wake with velocity and turbulence simulated by a three-dimensional (3D) fluid dynamic calculation. We apply the model to predict the aerosol distribution that would be generated by a propeller wake in the Stratospheric Controlled Perturbation Experiment (SCoPEx). We find that injecting 0.1 g s^{-1} calcite aerosol produces a nearly monodisperse plume and that at the same injection rate, condensable sulphate aerosol forms particles with average radii of 0.1 µm at 3 km downstream. We test the sensitivity of plume aerosol composition, size, and optical depth to the mass injection rate and injection location. Aerosol size distribution depends more strongly on injection rate than injection configuration. Comparing plume properties with specifications of a typical photometer, we find that plumes could be detected optically as the payload flies under the plume. These findings test the relevance of in situ sampling of aerosol properties by the SCoPEx outdoor experiment to enable quantitative tests of microphysics in a stratospheric plume. Our findings provide a basis for developing predictive models of SAI using aerosols formed in stratospheric aircraft wakes.

1 Introduction

Solar geoengineering, or Solar Radiation Modification (SRM), is the largescale intentional manipulation of Earth's radiative budget for the purpose of offsetting radiative forcing introduced by accumulating greenhouse gases. The introduction of aerosol or aerosol precursors to create an artificial reflective stratospheric aerosol layer, known as stratospheric aerosol injection (SAI), was identified as a promising form of SRM in the National Research Council report (2015). Current literature suggests that, coupled with emissions cuts, SAI could reduce increases in global mean temperature and extreme climate events (droughts and extreme precipitation) associated with increased greenhouse gas burdens. Recent works, including Irvine et al. (2016a, 2017, 2019) and Kravitz et al. (2013) detail these climatic effects and their global distributions.

SAI is contingent on the ability to artificially generate stratospheric aerosol. Several methods of transporting aerosol into the stratosphere have been considered in the literature, including artillery shells, hoses, balloons and aircraft (Battisti et al., 2009; Davidson et al., 2012). Of these, the release of aerosol or aerosol precursor from aircraft is considered both feasible and relatively inexpensive (Irvine et al., 2016b), therefore the remainder of this work will focus on understanding SAI in the context of aircraft injection. While many studies have examined stratospheric SRM in general circulation models, only two studies (Benduhn et al., 2016; Pierce et al., 2010) have simulated the creation of an aerosol plume from an aircraft. Both studies used zero-dimensional aerosol microphysics driven by the Turco and Yu (1997) plume dilution study. Observational data on aerosol behavior in stratospheric aircraft plumes is similarly limited (Fahey et al., 1993, 1995; Turco & Yu, 1997). More accurate predictions of the SAI aerosol distribution produced by aircraft will require better models that are tested and improved by more SAI-specific observations.

To effectively model the climate impacts of SAI, plume development from realistic injection scenarios must first be modelled, validated, and applied as initial conditions for global circulation models (GCMs). While the majority of current GCM studies represent SAI as a uniform solar reduction (Kravitz et al., 2011, 2013), a subset of models explicitly simulate aerosol microphysics, allowing size distributions to freely evolve (Dai et al., 2018; Simpson et al., 2019; Tilmes et al., 2009). However, even models with explicit aerosol microphysics implicitly assume that injected aerosol or aerosol precursors are instantaneously mixed into model grid boxes with horizontal scales of 100 km or greater. This approach neglects the near-field response, meaning the small-scale chemical and physical processes which would occur in aerosol plumes generated by aircraft. In the near field, the high concentration gradients which define a plume will drive non-linear microphysical processes and chemistry (Cameron et al., 2013). In some cases, near-field microphysics and chemistry will play an important role in determining the aerosol size distribution that mixes into the background stratosphere.

Three options for the generation of stratospheric aerosols have been proposed: (a) the release of gas phase SO_2 (b) the injection of H_2SO_4 gas to form accumulation mode (AM) H_2SO_4 aerosol (Pierce et al., 2010) or, (c) the injection of solid aerosols (e.g. calcite, diamond, alumina, titania) (Ferraro et al., 2011; Pope et al., 2012; Teller et al., 1996; Weisenstein et al., 2015).

The radiative efficiency, or the radiative forcing per injected aerosol mass, of sulphate aerosol is strongly size dependent. Backwards scattering efficiency decreases beyond an optimal radius of 150 nm, while gravitational particle settling increases with particle size. Heckendorn et al. (2009) found that injection of gas phase SO_2, which slowly oxidizes to form SO_3(g) before producing sulphate aerosol, tends to form particles with radii substantially larger than the optimal size ($r > 1\mu m$). This tendency serves to decrease the effective radiative cooling per unit mass of injected sulfur. Direct injection of AM- H_2SO_4, which immediately forms sulphate aerosol, to better control, or "steer," aerosol size distribution was proposed by Pierce et al. (2010). Only two studies, Pierce et al. (2010) and Benduhn et al. (2016), have looked at the near-field dynamics of the injection of AM- H_2SO_4 into an aircraft wake. Each of these used expanding plume models with nucleation and coagulation parameterizations for the H_2O- H_2SO_4 system which remain largely unvalidated for the high density, high temperature conditions of an aircraft wake. In both cases, a simulated high-density injection of AM- H_2SO_4 was allowed to develop until adequately diluted into pre-existing background particles, at which point the final sulphate aerosol size distribution was extracted.

Solid aerosols for SAI were first proposed by Teller et al. (1996), and a growing literature has looked at the use of solid engineered particles. Several studies have found that for the same radiative forcing, solid aerosols can produce less ozone loss, stratospheric heating and forward scattering as compared to sulfate aerosols (Ferraro et al., 2015; Keith et al., 2016; Pope et al., 2012; Weisenstein et al., 2015). However, no studies have investigated behavior of a high-density injection of solid particles on spatial scales relevant to aircraft injection.

GCM and two-dimensional (2D) global scale studies have investigated the impacts of introducing AM- H_2SO_4 as compared to SO_2(g). Findings of these works suggest that SAI using AM- H_2SO_4 may give better control of particle size and produce higher radiative efficiency relative to an SO_2(g) injection (Dai et al., 2018; Vattioni et al., 2019; Weisenstein et al., 2019). In the case of solid engineered particles, a global 2D chemical transport model has been used to predict climactic outcomes of SAI using injection of monodisperse solid aerosols (Keith et al., 2016; Weisenstein et al., 2015). All of these results, however, depend on the size distribution of

the aerosols injected into the grid-boxes of a global model, and in the case of solid aerosol or AM- H_2SO_4 that size distribution will be strongly dependent on plume-scale behavior.

Observations of stratospheric aerosol formation via gaseous SO_2 injection from volcanic eruptions and aircraft emissions provide information about the behavior of aerosols in the stratosphere and the largescale climatic impacts of point source injections (Friedl, 1997; Haywood et al., 2013; Proctor et al., 2018; Rahmes et al., 1998; Robock, 2000; Trenberth & Dai, 2007). However, data from volcanic eruptions do not strongly constrain estimates of response to continuous or non-point source injection and aircraft emissions exhaust sulfate in low concentrations compared to what would be expected if implementing SAI. In both cases, high concentrations of co-emitted constituents detract from the usefulness of the data, and neither observation relates to solid engineered particles. Therefore, these observations alone cannot effectively validate an SAI-like injection. Measurements in the exhaust plume of the Concorde aircraft highlighted uncertainties in the microphysics of the H_2O- H_2SO_4 aerosol system in an aircraft wake. Classical condensation and coagulation parameterizations were unable to replicate particle growth in the exhaust plume to achieve observed size distributions, and particle characteristics were highly sensitive to the homogeneous nucleation rate (Brown et al., 1996; Fahey et al., 1995; Kärcher et al., 1995). This prompted the theory that accounting for ion-mediated nucleation was necessary to accurately predict particle growth under high temperature conditions, although this has not been further validated (Yu & Turco, 1997). Datasets from convective events in the lower stratosphere and volcanic eruptions give insight into mid-field (10-1000 km) to global transport of aerosols, but do not provide information about near-field plume and particle dynamics. No direct observations of stratospheric AM- H_2SO_4 or solid aerosol exist to provide avenues for model validation.

Robust understanding of the microphysical processes of these materials will require the intentional co-development of model and observational experiments focused on constraining uncertainties of aerosol nucleation, condensation, evaporation and coagulation under SAI-like conditions in the stratosphere.

In this study we investigate aerosol growth dynamics using a 3D microphysical model driven by the velocity and turbulence fields from high-resolution computational fluid dynamics simulations. We base our simulation on the design of the Stratospheric Controlled Perturbation Experiment (SCoPEx) which was proposed by Dykema et al. (2014) to investigate aerosol microphysics in a turbulent wake and to collect information about catalytic chemistry and dynamics of the lower stratosphere (~20 km altitude). SCoPEx will use propellers to steer the payload and generate a region of turbulence into which aerosol or aerosol precursor will be injected. The payload will then navigate downstream to sample the plume at multiple locations.

We incorporate these design features in our model to study the injection of a solid aerosol and vapor-phase aerosol precursor from a balloon payload. We vary initial aerosol mass fluxes and examine the size distributions and optical detectability of produced plumes. We are particularly interested in the ability to produce a plume where the size distribution is representative of a radiatively efficient SAI deployment from an aircraft. Model inputs may be updated by the SCoPEx team with measured plume dynamical parameters to compare model and observations. In the concluding discussion we speculate about how this model may be applied to study SAI in aircraft plumes.

2 Model

Our modeling system is made up of three sub-models: (a) a commercial computational fluid dynamics (CFD) package to compute a 3D time invariant distribution of velocity and turbulent diffusion; (b) a MATLAB-based advection-diffusion scheme to carry aerosol through the CFD-derived velocity-diffusion fields; and (c) a sectional aerosol microphysical model that computes the evolution of the aerosol size distribution in each grid cell via nucleation, condensation and coagulation. All modeling apart from the CFD analysis used MATLAB 2017a, and all computations were run on the FASRC Cannon cluster.

2.1 CFD with ANSYS Fluent

The computational fluid dynamics (CFD) domain is constructed with ANSYS DesignModeler and meshed with ANSYS Meshing, both in the ANSYS Workbench package 17.2. Following the best practice guideline for CFD (Franke et al., 2004), the inlet and outlet of the domain should be at least 5*d* upstream and 15*d* downstream of the propellers, where *d* is the propeller diameter (1.9 m). The inlet is 20 m upstream and the outlet is 3000 m downstream, satisfying both requirements. The entire CFD domain is a cylinder of diameter 200 m and length 3 km. The domain consists of 12 million cells in an adaptive mesh, with the finest cell (0.025 m) in the vicinity and downstream of the propellers. The maximum cell expansion ratio is 1.2 to ensure no sudden change of the mesh resolution.

The simulation is conducted with the finite-volume solver ANSYS Fluent. We use a steady Reynolds-averaged Navier-Stokes (RANS) solver with the standard k-ε turbulence closure scheme. The SIMPLE (Semi-Implicit Method for Pressure-Linked Equations) algorithm is used for pressure-velocity coupling. The Least Squares Cell Based method is used for discretization of gradients, the Second Order scheme is used for discretization of pressure, and the Second Order Upwind scheme is used for discretization of momentum, turbulent kinetic energy and turbulent dissipation rate. The boundary conditions are: constant velocity of 1 ms^{-1} at the inlet, uniform reference (gauge) pressure of 0 Pa at the outlet, and free-slip at the outer surface. The propellers are modeled as 3D Fan Zones with 1.8 Pa pressure jump. The far-field ambient pressure is set at 5529 Pa and the fluid density is 0.0889 kg m^{-3}. These conditions simulate two propellers moving forward steadily at 1 m s^{-1} at an altitude of ~20 km.

2.2 Advection and Diffusion Model

Advection and diffusion are driven by the steady state velocity fields produced by Fluent. Velocities and diffusion coefficients are interpolated from the unstructured Fluent grid to the model grid using a Delaunay triangulation of the scattered sample points via MATLAB's scattered interpolant function, using a linear method. The algorithm is detailed by Amidror (2002).

The coefficients for turbulent diffusion are computed from turbulent viscosity using the standard ANSYS Schmidt number of 0.7. As described in the section above, we assume a stratosphere with laminar background flow of 1 ms^{-1}, and do not attempt to represent high intensity turbulence. All turbulence accounted for in this this model arises from motion of the propellers. This omission seems reasonable given the estimated waiting time of approximately 24 hours between turbulent encounters for a typical stratospheric air parcel (Vanneste, 2004). Balloon experiments, like SCoPEx, can likely avoid significant turbulence if isolated from lee waves, jet stream adjustments, and vigorous atmospheric convection.

To balance both the constraints required to achieve numerical stability and the need to resolve a small enough spatial scale to mimic injection from a nozzle, the desired domain of 3 km was broken into three nested grids. This allowed for high resolution at the nozzle "inlets" while keeping the simulation computationally tractable. Measured from the propeller, these regions are defined as: Box 1, from -3 to 6 m, with 0.1 m resolution, Box 2 from 6 to 100 m at 1 m resolution, and Box 3 from 100 to 3000 m with 3 m resolution. These boxes encompass the entire x dimension of the Fluent domain. Box boundaries are based on the average magnitude of the x-direction velocity, leveraging lower velocity values to increase the numerically stable spatial step, as detailed below.

We apply a second order accurate Lax-Wendroff advection scheme with a Superbee flux limiter to prevent spurious oscillations in locations with high velocity gradients while also preventing excessive numerical diffusion. 3D versions of this method were adapted from LeVeque (2002), and employed using logic outlined by Smaoui and Radi (2001). Operator splitting enabled the separate computation of diffusion across each time step. This was done using a simple 3D finite difference scheme as described by Hyman et al. (1997). The time steps for each domain were chosen to ensure that the Courant-Friedrichs-Lewy (CFL) value in each dimension did not exceed 0.8, and was, on average, substantially smaller. This value was chosen based on testing in Box 1, where we found a total domain mass error of 0.39% as compared to simulation with a maximum CFL equal to 0.065. This corresponded to timesteps of 0.008 s, 0.08 s and 0.9 s for Box 1, 2 and 3, respectively. The maximum diffusion coefficients of a given box were at most two orders of magnitude smaller than maximum velocity values in the same domain, such that achieving advection stability requirements ensured numerical stability of the diffusion scheme.

2.3 Sectional Aerosol Model

The nucleation, condensation and coagulation subroutines of the Atmospheric and Environmental Research (AER) 2-D chemical transport model (Weisenstein et al., 1997, 2006) were translated into MATLAB and coupled to the advection and diffusion code described above. They were applied, as discussed below, to separately analyze the continuous release of calcite ($CaCO_3$(s)), or sulfuric acid (H_2SO_4(g)), into the modeled propeller wake.

This model uses 40 logarithmically spaced sulfate aerosol bins, ranging in size from 3.9×10^{-4} to 3.2 µm, representing a doubling of particle volume from bin to bin. Solid calcite aerosol is represented by 8 sectional bins ranging from 0.28 to 2.8 µm, in which the number of monomers per particle is doubled between adjacent bins. Simulated sulfate aerosols are formed through homogeneous nucleation of H_2SO_4 and H_2O vapor, with explicit simulation of condensation, evaporation and coagulation (Weisenstein et al., 1997, 2006). Calcite aerosols are injected as monomers, and size distributions are modified only by coagulation among particles. This study did not include simultaneous injection of gaseous and solid species, and therefore only homogeneous coagulation is considered.

Because temperature, pressure, and relative humidity for this experiment are held constant, sulfate aerosol weight fraction is based on the total gas phase concentration of sulfuric acid at a given location. Aerosol composition is used to calculate the nucleation rate and critical cluster radius as presented in Vehkamäki (2002). High density injection of H_2SO_4(g) was found to exceed the validity range of the Vehkamäki nucleation rate parameterization of 10^{10} cm^{-3} s^{-1} in some spatial locations. To account for this, the AER nucleation module was modified to identify

locations where the concentration of sulfuric acid exceeds the threshold of barrierless kinetic particle formation, and to calculate the nucleation rate via the parameterizations of Määttänen et al. (2018). Following the precedent of Pierce et al. (2010), all sulfuric acid vapor is forced to condense if the nucleation rate exceeds the total particle density in a given spatial location.

The condensation and evaporation scheme, as given by Hamill and Yue (1980), and applied in the AER 2D model, are applied without modification. These processes are grouped into a subroutine which calculates the growth or loss of mass from a sulfate aerosol. The change in particle volume per second per surface area is determined from the sulfate aerosol weight fraction and surface vapor pressure, where a curvature correction for the Kelvin effect is included in the calculation (Weisenstein et al., 1997). The coagulation schemes derived and applied for sulfate and solid aerosol by Weisenstein et al. (1997, 2006, 2015) have been applied without modification.

3 Results

The advection-microphysics model configuration described above is applied to understand the near-field dynamics of calcite ($CaCO_3$) and sulfuric acid aerosol proposed for use in SCoPEx. As we explore in the concluding discussion, this problem is similar to the aerosol release into a stratospheric jet wake.

For the SCoPEx mission to provide observations relevant to SRM, it needs to produce downstream aerosols with radii within the range of roughly 0.2 to 1.0 µm. For calcite, the objective is to maintain a high fraction of the aerosol in monomer form, while for sulfate an ideal distribution would have a peak volume mean diameter (VMD) of 0.6 µm (Dykema et al., 2016). The least desirable outcome of the SCoPEx mission is to create particles substantially larger than these ideal sizes, as both particle lifetime and radiative efficiency decrease with increasing particle size. Generation of largely smaller than ideal particles, while imperfect for assessing radiative efficiency relevant to SAI, does not serve to increase particle sedimentation rates within the plume. Distributions centered on small particle sizes may continue to evolve beyond the domain of the study.

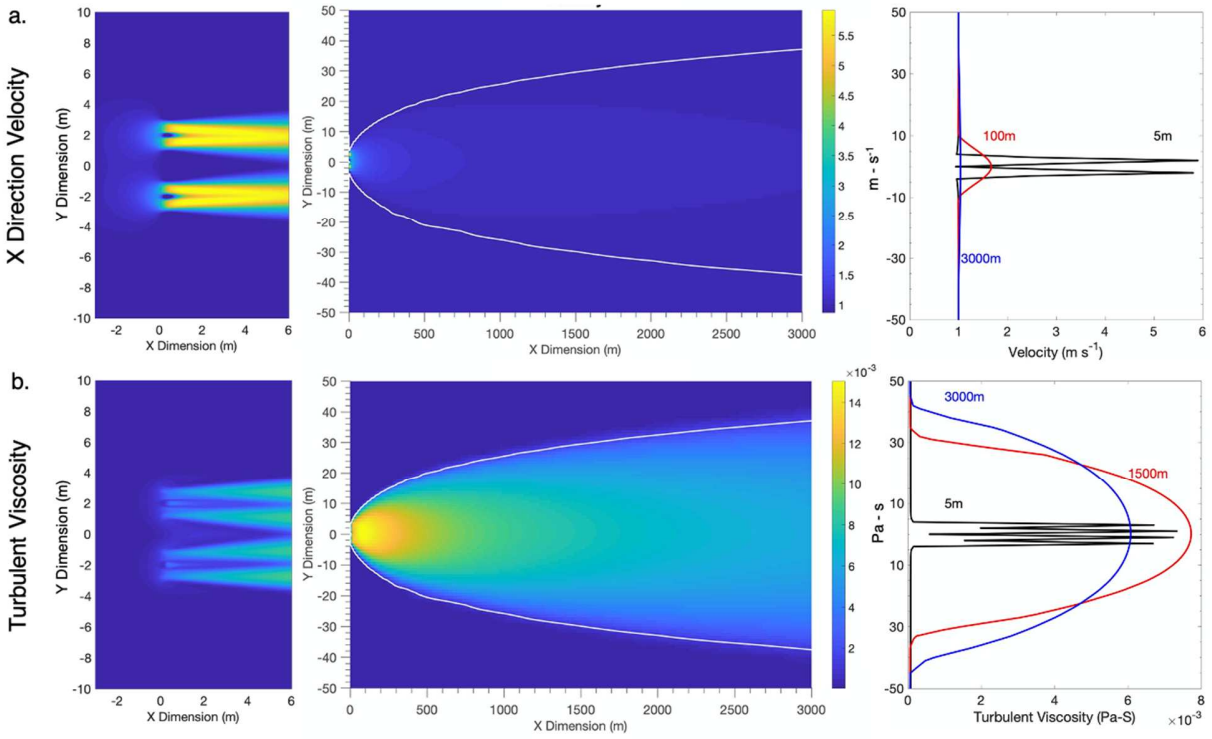

Figure 1. Shown above are the steady state x-direction velocity, u, and turbulent viscosity fields generated by ANSYS Fluent. Left panels show the genesis of disruptions to background x direction flow of 1 m s^{-1} at the inlets to two propellers, respectively located, at (0,2) and (0,-2) meters. The center panel shows the entire domain, from 0 to 3 km, where the imposed white line contours 1ms^{-1} in plot (a), and contours 10% of the absolute maximum turbulent viscosity in plot (b). Note Y direction scaling differs between the center and left panels. The right panel shows cross sections of velocity (a) and turbulent viscosity (b) through the Y plane at varying X locations.

The velocity and turbulent viscosity fields from the CFD simulation are shown in Figure 1. These fields form the basis of the simulation environment. We find peaks in x-direction velocity, u, directly downstream from the modeled propeller centers, with an absolute maximum value of 6.33 m s^{-1}. By 1500 m downstream from the inlet locations, the velocity is reduced to the imposed background flow of 1 m s^{-1}. Turbulent viscosity, used as a measure of particle mixing with background air, exhibits a narrow distribution of maximum values ~10 m downstream from simulated propellers. With increasing distance downstream, the spatial distribution of turbulent viscosity widens, attaining a full width at half maximum (FWHM) of 60 m by 1500 m downstream. Notably missing from these fields is the wake of the balloon itself, which is assumed to be sufficiently far from the payload to avoid wake crossing. Additionally, this simulation assumes a laminar stratospheric background flow, neglecting the potential impacts of breaking gravity waves. Results may be altered by initializing the CFD simulation with a higher turbulent ratio.

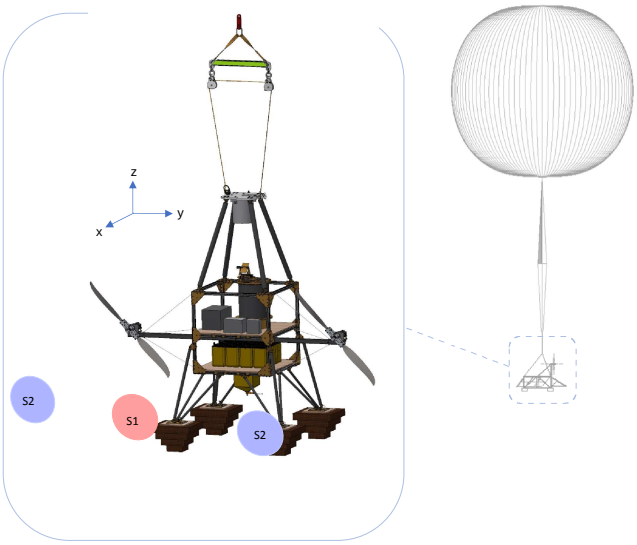

Figure 2. A simplified schematic of the proposed SCoPEx balloon and payload system. Potential injections scenarios 1 and 2 are shown in red and blue, respectively, as injections from the center of the system (S1), or the center of each propeller hub (S2).

The first challenge to achieving an accurate near-field delineation is the numerical representation of the physical injection nozzles. Currently, no literature provides technical specifications relevant to aerosolizing material for SAI. Leveraging ongoing laboratory studies, we assume that for SCoPEx, precipitated $CaCO_3$ powder with roughly monodisperse size distribution centered at ~0.5 µm volume mean diameter (VMD) will be aerosolized using the expansion of powder suspended in high pressure CO_2 through a 1-2 mm nozzle. Sulfuric acid vapor will be emitted from a heated reservoir through a nozzle of a few millimeter diameter. The millimeter-scale injector orifices are too small to directly resolve, instead we model injection as a 3D gaussian distribution of mass flux into the model grid, where the size of that distribution represents the scale of the nozzle spray pattern approximately 10 cm from the orifice. We use gaussian distributions with a full width at half maximum (FWHM) of 0.3 m and 1.0 m for the calcite and H_2SO_4 respectively.

The SCoPEx experiment team considered two configurations for the continuous injection of material from the payload (Figure 2): scenario 1 (S1), a single point injection between the propellers; and scenario 2 (S2), injection from the center of each propeller. While scenario 1 is the simplest to implement, we were not sure if it would adequately mix the material into a sufficiently large volume. Defining the plume "edge" as locations where the total particle number density drops below 1 cm^{-3}, we find plume diameter at 3 km to be insensitive to injection scenario for injection of both AM-H_2SO_4 and calcite. For sulphate, the FWHM (y-dimension diameter) of the plume is consistent across all scenarios and mass injection rates, with a value of 93 m. This suggests that injection at or between the propellers does not serve to greatly alter the characteristics of the particles' experienced velocity field. Calcite injection yields similar results, with an average plume FWHM of 70 m and a standard deviation of 3 m, or one spatial grid cell.

These findings support that scenario 1 is effective at dispersing material into the propeller wake. We also find that the final size distribution of particles within the plume is impacted by

injection location. Comparison between S1 and S2 across the same mass injection rate shows an average percent reduction in VMD at 3000 m of 11% and 16% for sulphate and calcite injection, respectively. The final size distribution of particles within the plume, while sensitive to location of injection, is more dependent on mass injection rate, as discussed in the next section. For this reason, the remainder of our results will focus on outcomes of an S1 injection.

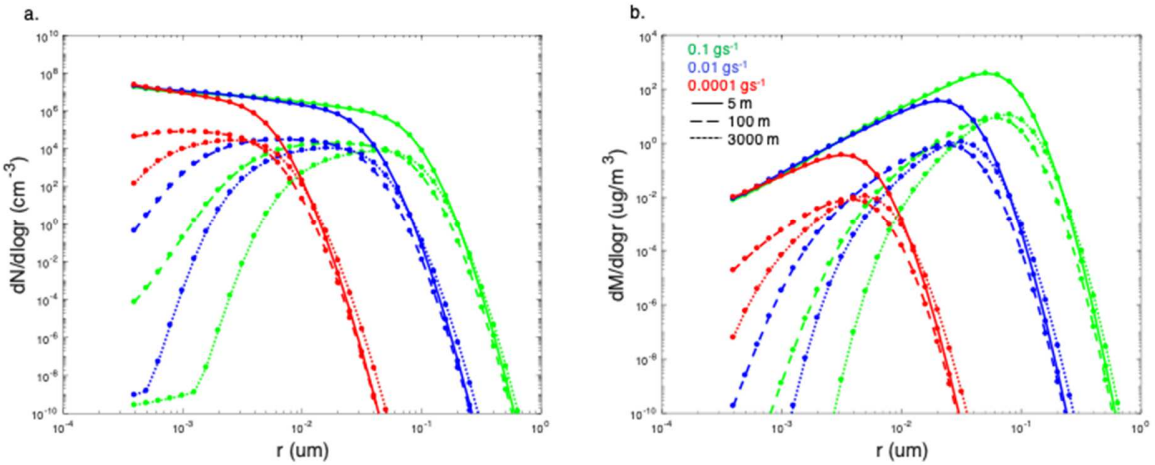

Figure 3. Steady state sulphate aerosol number (a) and mass (b) size distributions predicted by the AER model. Red, blue and green lines represent injection rates of 0.1, 0.01 and 0.0001 g s^{-1}, under Scenario 1, respectively. Solid, dashed and dotted lines represent average integrated aerosol number density and mass through the plume at sampling locations downstream of 5 m, 100 m and 3000 m, respectively.

Mass injection rates were varied by factors of 10 and 1000 to test the influence of initial particle number density on the final plume aerosol size distribution. These results (Figures 3, 4 and 5) show that particle size increases with injection rate and downstream location. Increasing the mass flux of H_2SO_4 from 0.0001 g s^{-1} to 0.1 g s^{-1}, reduces the negative skew of the downstream (3 km) size distribution by decreasing the share of smaller particles and shifting the distribution peak towards radii of ~0.1µm. Shifting calcite injection from 0.1 to 100 g s^{-1} similarly reduces the share of monomer particles in the final 100m of the plume to favor multi-monomer ($r > 0.275$ µm) aggregates (Figure 4). The differences in the resulting VMD of low vs. high initial mass fluxes, increase with distance downstream, or longer time in the system (Figure 5).

While findings for both materials follow the same trends, we rely on coagulation to promote particle growth when injecting gas phase H_2SO_4, whereas the objective of injecting 0.55 µm monomer calcite is to minimize coagulation between particles; to conserve monomer. Increasing initial mass flux of H_2SO_4 by a factor of 1000, from 0.0001 to 0.1 g s^{-1}, increases the number average particle radius at 3 km by 1500%, from 0.0025, to 0.04 µm, a desirable shift. Comparatively, the lowest calcite flux of 0.1 g s^{-1}, is the most desirable, maintaining 99% of the total mass in the final 100 m of the plume in monomer form. Increasing mass injection rate to 10 g $s^{-1}$and 100 g s^{-1}, with an S1 injection, shifts peak mass loading to favor particles of radii 0.5 and 0.75 µm, respectively.

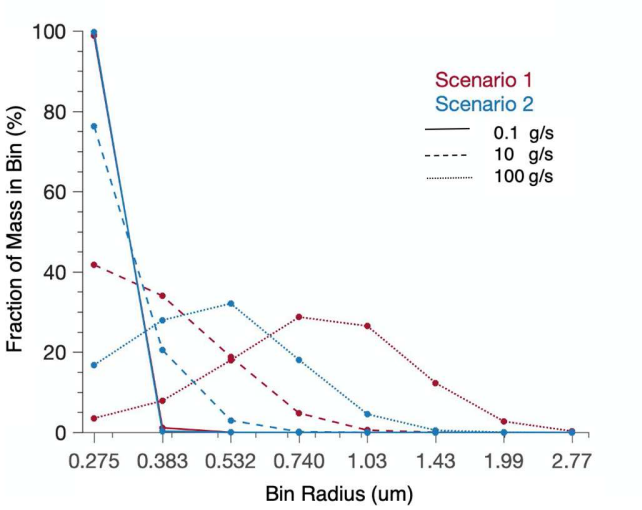

Figure 4. Calcite aerosol size distributions, shown as the fraction of total mass of in each sectional bin where the x-axis markers represent the central radius of each sectional size bin. These distributions represent the percent of total aerosol mass in the final 100 m of the plume across the full domain. Results are shown for three injection rates, 0.1 g s^{-1}, 10 g s^{-1}, and 100 g s^{-1}, for injection scenario 1 (red) and 2 (blue).

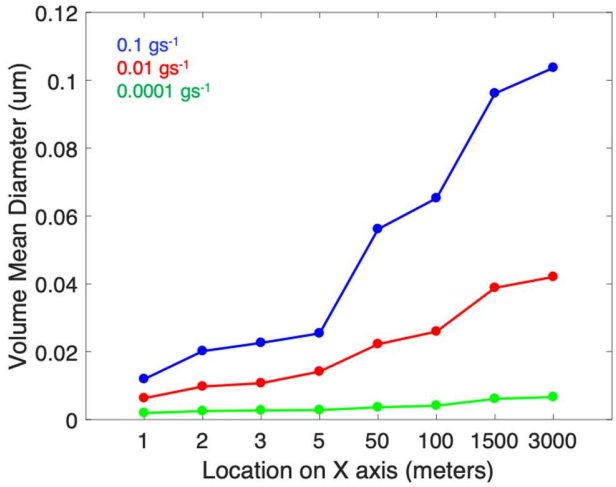

Figure 5. Steady state volume-mean particle diameter integrated over the y-z plane at increasing distances downstream from injection location. Results are shown for condensable H_2SO_4 injected via scenario 1 at rates 0.1, 0.01 and 0.0001 g s^{-1} as blue, red and green solid lines, respectively. In all cases a monotonic increase in average particle size is observed with distance downstream.

All tested mass injection rates display an increase in particle VMD with distance downstream. For sulphate, this results in particles with VMD of 0.006, 0.04, and 0.1 µm for injection rates of 0.0001, 0.01, and 0.1 g s^{-1}, respectively. This trend corroborates the notion that coagulation processes drive the final particle size distribution (Pierce et al., 2010). The relative differences in VMD between injection rates are the lowest closest to the nozzle, where

nucleation dominates, suggesting changes to nucleation rate are not driving changes in particle growth. After 6 m, virtually no gas phase H_2SO_4 remains in the system, such that further changes to particle size can only be due to particle coagulation. In Figure 5, the rate of change of VMD of the plume has significantly slowed by 1500 m, implying that the plume is disperse enough that coagulation between particles is no longer relevant. This finding tells us that to generate a sulphate plume with particle VMD of 0.6 µm, we must increase the initial mass injection rate; simply allowing the plume more time develop is unlikely to produce the desired result.

3.1 Optical Detection

Steady state number density distributions across the final domain were leveraged to investigate detectability of the plume. Using Mie scattering theory, the extinction optical depth was calculated by vertically integrating down columns in the y-z plane. Figure 6 shows the relative optical thickness of the sulphate and calcite aerosol plumes formed via scenario 1 with an injection rate of 0.1 g s^{-1}. Calcite exhibits greater optical thickness by an order of magnitude at 550 nm, with an average value of 8.6×10^{-4} and maximum of 0.014 across the domain, as compared to sulphate, with an average of 9.4×10^{-5} and maximum of 0.001.

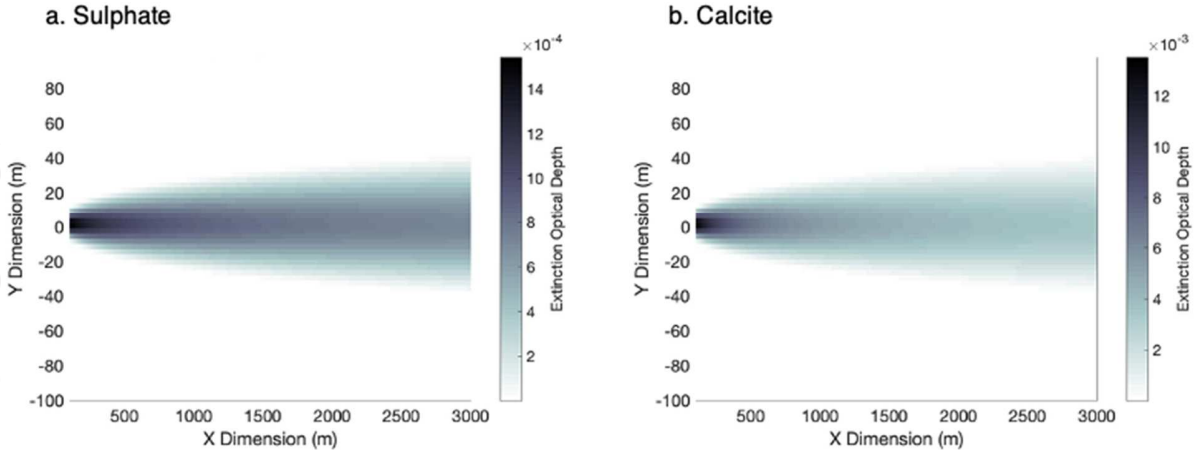

Figure 6. Extinction optical depth integrated vertically through all columns in the plume from 100-3000 m. Plots a and b show results for 0.1g s^{-1} injections of condensable H_2SO_4 and calcite, respectively. The resulting number density of calcite aerosol is 490 cm^{-3} on the centerline at a downstream distance of 1000 m, predominantly as monomers. At the same location, sulphate aerosol is present at a density of $2x10^5$ cm^{-3}. Aerosol optical depths were derived from Mie scattering theory at 550 nm, using refractive indices for sulphate and calcite stated in Dykema et al. (2016).

To better understand detectability of a theoretical plume against background stratospheric aerosol we extract a scattering measurement at 550 nm as could apply to observations from a narrowband, narrow field view photometer with azimuthal/zenith pointing capability. We assume an altitude of 21 km and solar elevation angle of 60° for a SCoPEx-like flight occurring at solar noon at 40°N during stratospheric turnaround. The observing instrument is assumed to be situated on the payload gondola (Figure 1), 200 m from the edge of the plume and positioned to

observe the plume 1 km downstream of the termination of a scenario 1 type injection of calcite aerosol.

Under these conditions, a notional photometer can employ established viewing geometries for measuring diffuse solar radiation (Torres et al., 2014). We assume that the gondola is physically located so it can scan the principal plane by altering its zenith pointing angle. By locating itself such that the plume is located at a zenith pointing angle of 20°, the ratio of the aerosol plume scattering to the background is maximized due to angular dependence of the corresponding scattering phase functions. The scattered radiation received by the photometer is proportional to product of the angular scattering coefficient (units of m^{-1} sr^{-1}), integrated along the line of sight, and the photometer field of view (in sr).

For an injection rate of 0.1 g s^{-1} and a vertical displacement of 200 m between the plume and the gondola, the ratio of the angular calcite scattering to the combined Rayleigh (molecular) and aerosol background angular scattering is about 10, when integrated over the line of sight. Assuming a photometer with a field of view comparable to that of Murphy et al. (2016) spanning a half-angle of 2.5° or 0.0065 sr, the expected scattered optical power incident on the photometer is about 15 nW. This level of optical power is about 5 orders of magnitude above the noise floor for a 1 ms integration time for compact, high-reliability optical detectors working at 550 nm. However, for this optical power the maximum achievable SNR is about 6000, due to photon shot noise. While a real instrument will achieve a reduced SNR due to optical and electrical inefficiencies, we expect adequate SNR to confidently detect the plume with a fast-scanning radiometer via the solar radiation it scatters.

4 Discussion and Conclusions

We found injection scenarios that allow the SCoPEx balloon experiment to generate sulfate or calcite aerosol plumes with size distributions that are relevant to understanding aerosol deployment in stratospheric aircraft wakes. Injection of gaseous H_2SO_4 with a mass injection rate of 0.1 g s^{-1} using a single injection location forms particles with a volume mean diameter of 0.1 µm, which are smaller than the ideal but large enough to be experimentally relevant. Injection of solid calcite at 0.1 g s^{-1} produces an almost perfectly monodisperse distribution.

Injection rate and injected material largely dictate the aerosol size distribution and optical thickness of the resulting plume. Plume diameter is largely determined by the fluid dynamics of the propeller wake and is insensitive to aerosol injection rate and location. In all cases, increasing mass injection rate increased the average optical thickness and the peak of particle size distribution of the plume. If injecting condensable H_2SO_4, larger mass injection rates favor the formation of accumulation mode particles, while low injection rates decrease total number density, limiting condensation and coagulation as mechanisms to grow particles. Alternatively, increasing mass injection rate of calcite tends to shift particle size distributions to favor aerosols consisting of two or more monomer units. Under the same injection strategy, a calcite plume exhibits significantly larger per mass scattering efficiency as compared to a plume generated via AM-H_2SO_4.

We find that the aerosol plumes in the SCoPEx wake could be detected by broad-band sun-angle-resolving photometer located just below the wake. The primary measurement of aerosol properties in SCoPEx will be by in situ aerosol instruments. Our scattering calculations suggest that these observations could be complimented by a small photometer mounted on the

SCoPEx gondola as it is maneuvered under the wake. This detection method may also be relevant to studies of aerosol formation in stratospheric aircraft plumes.

There are two important limitations to our study. First, our model incorporates Brownian coagulation, but omits gravitational and turbulent coagulation. In the latter case, particle inertia, impacting relative particle velocities, and wind field shear, would serve to increase particle collisions. These transport effects would likely dominate when the Stokes number is close to 1, and may only be a small concern given our background flow of 1 m s^{-1} (Benduhn, 2008; Riemer et al., 2007). For particle distributions less than 1 µm, Brownian coagulation largely dominates regardless of atmospheric turbulence, suggesting that these omissions are unlikely to have influenced outcomes of sulphate injection in which particle sizes largely remain below 1 µm. As particles become larger, the inertia of an individual particle within a flow field becomes significant and turbulent coagulation becomes relevant. Therefore, calcite distributions with particles larger than micrometer size are likely lacking coagulation kernel contributions from turbulent processes. Second, the calcite coagulation sticking coefficient was taken at a value of 1 but could have a real value anywhere between 0 and 1. These omissions and assumptions need to be tested and verified through iterations with observations and laboratory studies.

This work provides a foundation to use observations from SCoPEx or similar experiments to quantitively evaluate models of aerosol microphysics using observations. This modeling framework can be used in combination with (a) aerodynamic measurements, (b) lidar observations of plume extent, and, (c) in-situ particle size observations to constrain microphysical quantities such as the coagulation kernel. The overall goal would be to test models of aerosol microphysics by identifying weaknesses in the parameterizations of high-density aerosol nucleation, condensation and coagulation in a stratospheric wake. With adequate validation, this model can then be extended to model solar geoengineering deployment technologies from an aircraft. Such a study would need to extend nucleation parameterizations to include ion-induced nucleation and interaction of aerosol particles and precursors with other species from the effluent streams in the aircraft wake. This would naturally build on the work of Pierce et al. (2010) and Benduhn et al. (2016), in the context of condensable H_2SO_4, and extend findings to solid aerosols, like calcite.

Iteration between model development and observations of stratospheric aerosol formation will be needed to provide more accurate near-field predictions of aerosol properties used to initialize global models of stratospheric response to aerosol solar geoengineering.

Acknowledgments

This work was funded by Harvard's Solar Geoengineering Research Program. Thanks to Debra Weisenstein for assistance adapting the aerosol microphysics methods from the AER 2D model, Guiseppe Torri for his numerical advection guidance, and Craig Mascarenhas for extracting data from Fluent. The computations in this paper were run on the FASRC Cannon cluster supported by the FAS Division of Science Research Computing Group at Harvard University. Data generated and investigated in this work are openly available on Harvard Dataverse (https://doi.org/10.7910/DVN/JMHKFT).

References

Amidror, I. (2002). Scattered data interpolation methods for electronic imaging systems: a survey. *Journal of Electronic Imaging*, *11*(2), 157–176. https://doi.org/10.1117/1.1455013

Battisti, D., Blackstock, J. J., Caldeira, K., Eardley, D. E., Katz, J. I., Keith, D. W., et al. (2009). Climate engineering responses to climate emergencies. *IOP Conference Series: Earth and Environmental Science*, *6*(45), 452015. https://doi.org/10.1088/1755-1307/6/45/452015

Benduhn, F. (2008). *Implications of aerosol growth dynamics and aerosol-cloud interaction to the Sun-cloud-climate hypothesis*. University of Hamburg.

Benduhn, F., Schallock, J., & Lawrence, M. G. (2016). Early growth dynamical implications for the steerability of stratospheric solar radiation management via sulfur aerosol particles: Steerability of Stratospheric SRM. *Geophysical Research Letters*, *43*(18), 9956–9963. https://doi.org/10.1002/2016GL070701

Brown, R. C., Miake-Lye, R. C., Anderson, M. R., Kolb, C. E., & Resch, T. J. (1996). Aerosol dynamics in near-field aircraft plumes. *Journal of Geophysical Research: Atmospheres*, *101*(D17), 22939–22953. https://doi.org/10.1029/96JD01918

Cameron, M. A., Jacobson, M. Z., Naiman, A. D., & Lele, S. K. (2013). Effects of plume-scale versus grid-scale treatment of aircraft exhaust photochemistry: EFFECTS OF PLUME VERSUS GRID SCALE. *Geophysical Research Letters*, *40*(21), 5815–5820. https://doi.org/10.1002/2013GL057665

Dai, Z., Weisenstein, D. K., & Keith, D. W. (2018). Tailoring Meridional and Seasonal Radiative Forcing by Sulfate Aerosol Solar Geoengineering. *Geophysical Research Letters*, *45*(2), 1030–1039. https://doi.org/10.1002/2017GL076472

Davidson, P., Burgoyne, C., Hunt, H., & Causier, M. (2012). Lifting options for stratospheric aerosol geoengineering: advantages of tethered balloon systems. *Philosophical Transactions of the Royal Society A: Mathematical, Physical and Engineering Sciences*, *370*(1974), 4263–4300. https://doi.org/10.1098/rsta.2011.0639

Dykema, J. A., Keith, D. W., Anderson, J. G., & Weisenstein, D. (2014). Stratospheric controlled perturbation experiment: a small-scale experiment to improve understanding of the risks of solar geoengineering. *Philosophical Transactions of the Royal Society A: Mathematical, Physical and Engineering Sciences*, *372*(2031), 20140059–20140059. https://doi.org/10.1098/rsta.2014.0059

Dykema, J. A., Keith, D. W., & Keutsch, F. N. (2016). Improved aerosol radiative properties as a foundation for solar geoengineering risk assessment: NEED FOR ACCURATE AEROSOL PROPERTIES FOR SRM. *Geophysical Research Letters*, *43*(14), 7758–7766. https://doi.org/10.1002/2016GL069258

Fahey, D. W., Kawa, S. R., Woodbridge, E. L., Tin, P., Wilson, J. C., Jonsson, H. H., et al. (1993). In situ measurements constraining the role of sulphate aerosols in mid-latitude ozone depletion. *Nature*, *363*(6429), 509–514. https://doi.org/10.1038/363509a0

Fahey, D. W., Keim, E. R., Woodbridge, E. L., Gao, R. S., Boering, K. A., Daube, B. C., et al. (1995). In situ observations in aircraft exhaust plumes in the lower stratosphere at midlatitudes. *Journal of Geophysical Research*, *100*(D2), 3065. https://doi.org/10.1029/94JD02298

Ferraro, A. J., Highwood, E. J., & Charlton-Perez, A. J. (2011). Stratospheric heating by potential geoengineering aerosols. *Geophysical Research Letters*, *38*(24), n/a-n/a. https://doi.org/10.1029/2011GL049761

Ferraro, A. J., Charlton-Perez, A. J., & Highwood, E. J. (2015). Stratospheric dynamics and midlatitude jets under geoengineering with space mirrors and sulfate and titania aerosols. *Journal of Geophysical Research: Atmospheres*, *120*(2), 414–429. https://doi.org/10.1002/2014JD022734

Franke, J., Hirsch, C., Jensen, A., Krüs, H., Schatzmann, M., Westbury, P., et al. (2004). Recommendations on the use of CFD in wind engineering. *Proceedings of the International Conference on Urban Wind Engineering and Building Aerodynamics*.

Friedl, R. (1997). *Atmospheric Effects of Subsonic Aircraft: Interim Assessment Report of the Advanced Subsonic Technology Program* (Reference Publication No. 97B00048) (p. 168). Washington, D.C.: National Aeronautics and Space Administration. Retrieved from https://ntrs.nasa.gov/citations/19970022603

Haywood, J. M., Jones, A., Bellouin, N., & Stephenson, D. (2013). Asymmetric forcing from stratospheric aerosols impacts Sahelian rainfall. *Nature Climate Change*, *3*(7), 660–665. https://doi.org/10.1038/nclimate1857

Heckendorn, P., Weisenstein, D., Fueglistaler, S., Luo, B. P., Rozanov, E., Schraner, M., et al. (2009). The impact of geoengineering aerosols on stratospheric temperature and ozone. *Environmental Research Letters*, *4*(4), 045108. https://doi.org/10.1088/1748-9326/4/4/045108

Hyman, J., Shashkov, M., & Steinberg, S. (1997). The Numerical Solution of Diffusion Problems in Strongly Heterogeneous Non-isotropic Materials. *Journal of Computational Physics*, *132*(1), 130–148. https://doi.org/10.1006/jcph.1996.5633

Irvine, P., Emanuel, K., He, J., Horowitz, L. W., Vecchi, G., & Keith, D. (2019). Halving warming with idealized solar geoengineering moderates key climate hazards. *Nature Climate Change*, *9*(4), 295–299. https://doi.org/10.1038/s41558-019-0398-8

Irvine, P. J., Kravitz, B., Lawrence, M. G., & Muri, H. (2016a). An overview of the Earth system science of solar geoengineering. *Wiley Interdisciplinary Reviews: Climate Change*, *7*(6), 815–833. https://doi.org/10.1002/wcc.423

Irvine, P. J., Kravitz, B., Lawrence, M. G., & Muri, H. (2016b). An overview of the Earth system science of solar geoengineering: Overview of the earth system science of solar geoengineering. *Wiley Interdisciplinary Reviews: Climate Change*, *7*(6), 815–833. https://doi.org/10.1002/wcc.423

Irvine, P. J., Kravitz, B., Lawrence, M. G., Gerten, D., Caminade, C., Gosling, S. N., et al. (2017). Towards a comprehensive climate impacts assessment of solar geoengineering. *Earth's Future*, *5*(1), 93–106. https://doi.org/10.1002/2016EF000389

Kärcher, B., Peter, Th., & Ottmann, R. (1995). Contrail formation: Homogeneous nucleation of H_2SO_4/H_2O droplets. *Geophysical Research Letters*, *22*(12), 1501–1504. https://doi.org/10.1029/95GL01337

Keith, D. W., Weisenstein, D. K., Dykema, J. A., & Keutsch, F. N. (2016). Stratospheric solar geoengineering without ozone loss. *Proceedings of the National Academy of Sciences*, *113*(52), 14910–14914. https://doi.org/10.1073/pnas.1615572113

Kravitz, B., Robock, A., Boucher, O., Schmidt, H., Taylor, K. E., Stenchikov, G., & Schulz, M. (2011). The Geoengineering Model Intercomparison Project (GeoMIP). *Atmospheric Science Letters*, *12*(2), 162–167. https://doi.org/10.1002/asl.316

Kravitz, B., Caldeira, K., Boucher, O., Robock, A., Rasch, P. J., Alterskjaer, K., et al. (2013). Climate model response from the Geoengineering Model Intercomparison Project (GeoMIP). *Journal of Geophysical Research: Atmospheres*, *118*(15), 8320–8332. https://doi.org/10.1002/jgrd.50646

LeVeque, R. J. (2002). *Finite volume methods for hyperbolic problems*. Cambridge ; New York: Cambridge University Press.

Murphy, D. M., Telg, H., Eck, T. F., Rodriguez, J., Stalin, S. E., & Bates, T. S. (2016). A miniature scanning sun photometer for vertical profiles and mobile platforms. *Aerosol Science and Technology*, *50*(1), 11–16. https://doi.org/10.1080/02786826.2015.1121200

National Research Council (U.S.), National Research Council (U.S.), & National Research Council (U.S.) (Eds.). (2015). Overview of the Albedo Modification Assessment. In *Climate intervention: reflecting sunlight to cool earth* (pp. 43–44). Washington, D.C: The National Academy Press.

Pierce, J. R., Weisenstein, D. K., Heckendorn, P., Peter, T., & Keith, D. W. (2010). Efficient formation of stratospheric aerosol for climate engineering by emission of condensible vapor from aircraft: AEROSOL FROM CONDENSIBLE VAPOR. *Geophysical Research Letters*, *37*(18), n/a-n/a. https://doi.org/10.1029/2010GL043975

Pope, F. D., Braesicke, P., Grainger, R. G., Kalberer, M., Watson, I. M., Davidson, P. J., & Cox, R. A. (2012). Stratospheric aerosol particles and solar-radiation management. *Nature Climate Change*, *2*(10), 713–719. https://doi.org/10.1038/nclimate1528

Proctor, J., Hsiang, S., Burney, J., Burke, M., & Schlenker, W. (2018). Estimating global agricultural effects of geoengineering using volcanic eruptions. *Nature*, *560*(7719), 480–483. https://doi.org/10.1038/s41586-018-0417-3

Rahmes, T. F., Omar, A. H., & Wuebbles, D. J. (1998). Atmospheric distributions of soot particles by current and future aircraft fleets and resulting radiative forcing on climate. *Journal of Geophysical Research: Atmospheres*, *103*(D24), 31657–31667. https://doi.org/10.1029/98JD02815

Riemer, N., Wexler, A. S., & Diehl, K. (2007). Droplet growth by gravitational coagulation enhanced by turbulence: Comparison of theory and measurements. *Journal of Geophysical Research*, *112*(D7), D07204. https://doi.org/10.1029/2006JD007702

Robock, A. (2000). Volcanic eruptions and climate. *Reviews of Geophysics*, *38*(2), 191–219. https://doi.org/10.1029/1998RG000054

Simpson, I. R., Tilmes, S., Richter, J. H., Kravitz, B., MacMartin, D. G., Mills, M. J., et al. (2019). The Regional Hydroclimate Response to Stratospheric Sulfate Geoengineering and the Role of Stratospheric Heating. *Journal of Geophysical Research: Atmospheres*, *124*(23), 12587–12616. https://doi.org/10.1029/2019JD031093

Smaoui, H., & Radi, B. (2001). Comparative study of different advective schemes: Application to the MECCA model. *Environmental Fluid Mechanics*, *1*(4), 361–381. https://doi.org/10.1023/A:1015764813423

Teller, E., Wood, L. T., & Hyde, R. A. (1996). Global warming and ice ages: I. prospects for physics based modulation of global change.

Tilmes, S., Garcia, R. R., Kinnison, D. E., Gettelman, A., & Rasch, P. J. (2009). Impact of geoengineered aerosols on the troposphere and stratosphere. *Journal of Geophysical Research*, *114*(D12), D12305. https://doi.org/10.1029/2008JD011420

Torres, B., Dubovik, O., Toledano, C., Berjon, A., Cachorro, V. E., Lapyonok, T., et al. (2014). Sensitivity of aerosol retrieval to geometrical configuration of ground-based sun/sky radiometer observations. *Atmospheric Chemistry and Physics*, *14*(2), 847–875. https://doi.org/10.5194/acp-14-847-2014

Trenberth, K. E., & Dai, A. (2007). Effects of Mount Pinatubo volcanic eruption on the hydrological cycle as an analog of geoengineering. *Geophysical Research Letters*, *34*(15). https://doi.org/10.1029/2007GL030524

Turco, R. P., & Yu, F. (1997). Aerosol invariance in expanding coagulating plumes. *Geophysical Research Letters*, *24*(10), 1223–1226. https://doi.org/10.1029/97GL01092

Vanneste, J. (2004). Small-Scale Mixing, Large-Scale Advection, and Stratospheric Tracer Distributions. *Journal of the Atmospheric Sciences*, *61*(22), 2749–2761. https://doi.org/10.1175/JAS3303.1

Vattioni, S., Weisenstein, D., Keith, D., Feinberg, A., Peter, T., & Stenke, A. (2019). Exploring accumulation-mode H_2SO_4 versus SO_2 stratospheric sulfate geoengineering in a sectional aerosol–chemistry–climate model. *Atmospheric Chemistry and Physics*, *19*(7), 4877–4897. https://doi.org/10.5194/acp-19-4877-2019

Weisenstein, D., Keith, D., Visioni, D., & Henning, F. (2019, December). *GeoMIP Test Bed Experiment: Injection of Accumulation Mode H2SO4 Particles in Chemistry-Climate Models*. Poster presented at the AGU Fall Meeting, San Francisco, CA.

Weisenstein, D. K., Keith, D. W., & Dykema, J. A. (2015). Solar geoengineering using solid aerosol in the stratosphere. *Atmospheric Chemistry and Physics*, *15*(20), 11835–11859. https://doi.org/10.5194/acp-15-11835-2015

Weisenstein, Debra K., Yue, G. K., Ko, M. K. W., Sze, N.-D., Rodriguez, J. M., & Scott, C. J. (1997). A two-dimensional model of sulfur species and aerosols. *Journal of Geophysical Research: Atmospheres*, *102*(D11), 13019–13035. https://doi.org/10.1029/97JD00901

Yu, F., & Turco, R. P. (1997). The role of ions in the formation and evolution of particles in aircraft plumes. *Geophysical Research Letters*, *24*(15), 1927–1930. https://doi.org/10.1029/97GL01822